Case Studies in Construction Materials 22 (2025) e04718

Contents lists available at ScienceDirect

Case Studies in Construction Materials

journal homepage: www.elsevier.com/locate/cscm

Effects of Key 3D concrete printing process parameters on layer shape: Experimental study and Smooth Particle Hydrodynamics modelling

Dong An, Mahfuzur Rahman, Y.X. Zhang, Richard (Chunhui) Yang *

Centre for Advanced Manufacturing Technology, School of Engineering, Design and Built Environment, Western Sydney University, Locked Bag 1797, Penrith, NSW 2751, Australia

ARTICLE INFO

Keywords:
3D concrete printing (3DCP)
Smooth Particle Hydrodynamics (SPH)
Layer shape
Inter-layer deformation
Rheological behaviours

ABSTRACT

3D concrete printing (3DCP) is an innovative technology with significant potential in construction. However, it faces critical challenges in achieving precise layer geometry and dimensional accuracy, as small geometric deviations in individual layers can compromise the stability and performance of the entire structure. To investigate the underlying deformation mechanisms, this study develops an integrated analysis framework combining experimental study with Smooth Particle Hydrodynamics (SPH) modelling. Key rheological and process parameters for 3DCP are identified experimentally. For the first time, a novel three-dimensional (3-D) SPH model is devised to simulate single- and double-layer concrete printing processes, considering nozzle moving speed, material inlet speed, and nozzle height. The high consistency between experimental and SPH results demonstrates the accuracy of models in predicting layer shape and tracking inter-layer deformations. Parametric analysis reveals a self-compensatory effect of nozzle height on layer height variations and demonstrates that a lower nozzle speed to material inlet velocity ratio improves layer shape and structural performance. These findings provide insights into the control of construction materials to enhance printing quality and structural reliability in 3DCP.

1. Introduction

Three-dimensional concrete printing (3DCP) is an innovative construction technique that builds structures by extruding concrete layer by layer without using traditional formwork [1]. This technique gained a wide range of attention from both academia and industry due to its potential to reduce costs, labour, and construction time while allowing the creation of structures with complex geometry and shape [2,3]. Despite these benefits, 3D printed concrete components often suffer from subpar surface finishes and limited dimensional accuracy. These issues are generated due to the absence of formwork and challenges in controlling the geometry of each printed layer [4,5]. Geometric discrepancies introduced in a single layer tend to accumulate over subsequent layers, propagating imperfections from individual filaments to the entire structure. This can impact the aesthetics, stability, mechanical strength, and durability of 3D printed concrete structures [6,7].

To improve geometric precision in 3DCP, researchers have investigated material behaviours and process parameters to identify key

* Corresponding author.
E-mail address: R.Yang@westernsydney.edu.au (R.(C. Yang).

https://doi.org/10.1016/j.cscm.2025.e04718
Received 13 February 2025; Received in revised form 23 April 2025; Accepted 29 April 2025
Available online 30 April 2025

factors affecting printed layer shapes and deformations. Fresh concrete was commonly treated as a shear-thinning Bingham fluid. Among its rheological properties, yield stress plays a key role in shaping the extruded materials [8]. The shear thinning affects filament shape while viscosity has a minimal influence [9,10]. Among 3DCP process parameters, two critical ratios were identified: the ratio of nozzle diameter to nozzle height, and the ratio of nozzle travel speed to material inlet velocity [10,11]. Keeping these ratios near 1 can prevent filament buckling and tearing. Larger nozzle diameters and higher material inlet velocities create flatter, more rectangular filaments, while smaller nozzles increase stress concentrations, raising the risk of damage and tearing [8]. Furthermore, extrusion forces induce substrate deformation, leading to lateral flow and structural instability [11–13]. While most studies have focused on single-layer printing, multi-layer printing remains underexplored due to the complexity of interlayer interactions. In multi-layer printing, accumulated inter-layer deformations can significantly alter the structural geometry and stability [14]. The process parameter–layer geometry relationships derived from single-layer studies cannot be applied to multi-layer cases, as the printing substrate changes from a rigid print bed to a deformable printed layer with varying stiffness, surface profile, and interfacial friction. These differences influence material deposition and structural integrity. A key challenge is understanding how deformation and geometric discrepancies propagate across layers, ultimately affecting the dimensional accuracy and stability of printed structures.

Given these challenges, accurately predicting layer shape is essential for ensuring structural precision and minimising cumulative deformation. However, traditional trial-and-error methods are impractical for large-scale construction due to their resource-intensive and time-consuming nature. To overcome these limitations, various numerical techniques were applied to simulate the 3D printing process [15–17], with a focus on two-dimensional (2-D) modelling. Comminal, et al. [11] developed computational fluid dynamic (CFD) models using a generalised Newtonian model and the elastic-viscoplastic model to characterise the rheological behaviours of fresh concrete. Cheng et al. [18] developed the reproducing kernel particle method (RKPM) to simulate concrete slump tests and 3D printing process. However, their approach involved extruding material from a long nozzle, causing high fluid pressure and excessive initial material inlet speed. Reinold, et al. [12,19] devised the Particle Finite Element Method (PFEM) to simulate the extrusion process, using an elastic-viscoplastic constitutive model based on a unified fluid and solid mechanics formulation. However, the need for frequent re-meshing to prevent element distortion increased computational costs, limiting these simulations only to 2-D models. To address this, Rizzieri et al. [20,21] introduced a mesh de-refinement technique to reduce the number of degrees of freedom in time. However, those 2-D models could only simulate the printing of printing direction and only suit the infinite brick-type extrusion from rectangular nozzles [22]. To break the limitation, Yu et al. [23] developed a 2-D virtual printing scheme using the Smooth Particle Hydrodynamics (SPH) method, where the widely applied circular nozzle was simulated, and the lateral layer deformation was accurately captured. However, this model solely predicts cross-sectional shape and cannot account for the material flow along the printing direction. To this end, this study proposes a novel 3D SPH model which simulates concrete motion along the printing direction and captures inter-layer deformations. Compared to 2D models, it enables more realistic geometry predictions by capturing complete shapes and multi-directional deformation of extruded materials.

While most numerical studies have focused on single-layer shape prediction, only a few [18,24] have explored double-layer printing, often using specimens primarily for model validation without thoroughly examining the associated deformations. However, double-layer modelling is crucial due to the introduction of new boundary conditions that affect material deposition and structural stability [14]. The complexity of simulating layer-to-layer deformation under varying process parameters presents considerable computational challenges, deterring comprehensive investigation. To the authors' knowledge, no studies have yet examined the numerical prediction of layer dimensions for double-layer 3DCP with varying process parameters. To bridge this gap, this study develops a 3D SPH model to simulate single- and double-layer 3DCP, predicting layer geometries validated using experimental data.

SPH method as a mesh-free, Lagrangian particle approach is naturally well-suited for fluid flow problems involving large deformations and free surfaces, which are commonly encountered in 3DCP [25]. It avoids mesh distortion and the need for re-meshing in Lagrangian mesh methods like PFEM, as well as the computational inefficiencies caused by the hollow mesh of Eulerian methods like CFD. The SPH method has been proven effective in modelling the flow of viscous fluids, such as self-consolidating cementitious composites [26–28] and 3D printable fibre-reinforced polymer composites [29,30].

To fill in the aforementioned research gaps, in this study, the integrated analysis framework with the experimental studies and 3-D SPH modelling of 3DCP is developed. In the experimental work, rheological tests are performed to determine key parameters of fresh concrete including static and dynamic yield stresses and viscosity, which are used to define the material model in the SPH model. 3DCP tests are performed to print single-layer and double-layer concrete samples and their cross-sectional shapes are characterised. In the numerical work, the novel 3-D SPH model is devised to simulate both single-layer and double-layer 3D concrete printing and predict the layer shape. The experimental results are utilised to validate these numerical models. Furthermore, through a parametric study, the devised 3-D SPH models are employed to investigate the influences of two key processing parameters, the ratio of the nozzle moving velocity to material inlet velocity and the nozzle height, on layer shape and inter-layer deformations. This paper is outlined in four sections. Section 2 details the development of integrated analysis framework with the experimental study and 3-D SPH modelling of 3DCP including rheological and 3DCP tests, and the numerical models using the 3-D SPH method. Section 3 provides the results and discussion on comparing of the experimental and numerical results and conducting a parametric study to investigate the influences of the two key processing parameters on layer shape and inter-layer deformation. Finally, Section 4 draws conclusions, indicates the limitations of current SPH modelling approach, and provides recommendations for future work.

2. Methodology

2.1. Development of the integrated analysis framework with experimental study and 3-D SPH numerical modelling for 3DCP

Fig. 1 illustrates the integrated analysis framework with the experimental study and 3-D SPH numerical modelling for 3DCP developed in this study, in which the experimental studies and the 3-D SPH modelling and simulations are interlinked via data flows to form the integrated analysis process. In the experimental studies, firstly, a series of rheological tests were performed to determine key parameters of fresh concrete, including static and dynamic yield stresses and viscosity. The obtained data were then used to define its material model in the 3-D SPH model. Secondly, 3DCP tests were performed to print ten concrete segments: five single-layer samples and five double-layer samples, whose cross-sectional shapes were measured and characterised. In the numerical modelling and simulations, at the first time, the novel 3-D SPH model was devised to simulate both single-layer and double-layer 3D concrete printing processes and predict the layer shapes of 3D printed concrete samples. The experimental results of 3-D printed concrete samples were utilised to validate these numerical models. Furthermore, through parametric studies, the devised 3-D SPH numerical models were further employed to investigate the influences of two key processing parameters, the ratio of the nozzle moving velocity V_n to material inlet velocity V_m and the nozzle height, on layer shape and inter-layer deformations.

2.2. Experimental design and procedure

2.2.1. Materials

The cement-based mortar used in the 3DCP experiment was formulated with a binder system consisting of Ordinary Portland Cement (OPC), conforming to AS 3972 Type GP, ground granulated blast-furnace slag (GGBFS), and silica fume (SF) with fine sand (max. Particle size: 1.18 mm). The binder composition was 30 % cement, 60 % GGBFS, and 10 % SF. The water to binder ratio is 0.25 and the sand to binder ratio is 0.36. Furthermore, a polycarboxylate-based high-range water reducer admixture (5 L/m^3) and a Viscosity-Modifying Agent (8 L/m^3) were used to modify the rheology of mortar, reducing yield stress and viscosity while improving workability and water retention. These admixture dosages were optimised using a Taguchi method to achieve a flowability range of 30 ~ 40 mm. The mix was designed for a relatively long open time and excellent early-age strength to ensure its printability.

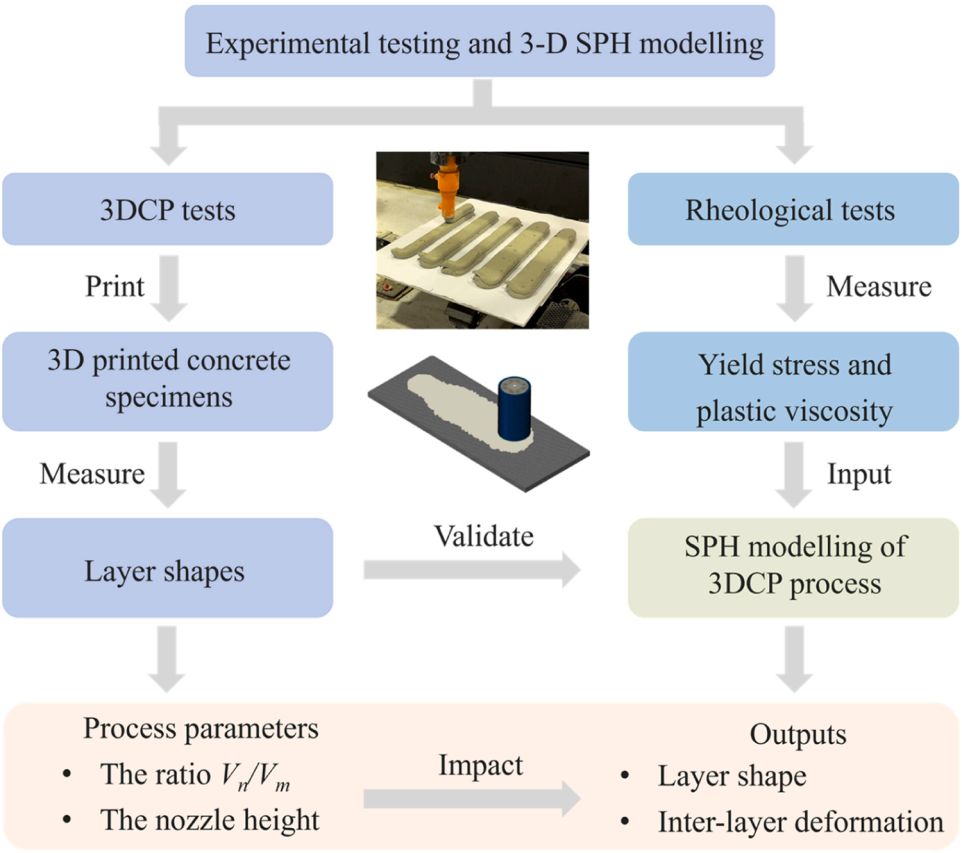

Fig. 1. Integrated analysis framework with the experimental study and SPH numerical modelling of 3DCP.

2.2.2. Rheological test

The rheological behaviours of the mortar were measured using an International Centre for Aggregate Research (ICAR) Plus rheometer. The setup included a cylindrical container holding the fresh mortar, a multiple blade vane driven by an electric motor to shear the mortar, and a torque meter. The multiple blade vane was chosen for its ability to generate a uniform flow velocity profile, ensuring accurate and stable flow curve measurements. To prevent slippage along the container walls, the container featured vertical rods around its perimeter [31].

Dynamic and static yield stresses, as well as plastic viscosity, were measured on three mortar batches at 15 minutes, coinciding with the time of extrusion. Dynamic yield stress and plastic viscosity were determined using a flow curve test, which included a pre-shear period followed by a series of flow measurements. During the pre-shear, the vane rotated at a maximum speed of 0.6 rev/s to break down any thixotropic structures and create a consistent shearing history. The rotation speed was then gradually reduced from 0.6 to 0.03 rev/s, with the vane speed held constant for 5 seconds at each step, during which the average speed and torque were recorded.

Static yield stress was measured using constant shear rate tests, where the vane rotated at 0.025 rev/s. As the torque increased over time, the maximum torque recorded was used to calculate the static yield stress.

2.2.3. Sample fabrication using 3DCP

The experimental 3D printing was conducted using a desktop 3D printer (3D PotterBot Super 10 with the auger system). This printer features a print bed that can move biaxially in the horizontal direction, an auger screw assembly that can move vertically, and a nozzle with a diameter of 25.4 mm (Fig. 2).

The 3DCP tests involved printing five single-layer and five double-layer mortar specimens with varying processing parameters, including the nozzle move velocity V_n, material inlet velocity V_m and nozzle height H_{nozzle} as detailed in Table 1. A schematic of the 3DCP test configuration is shown in Fig. 3. In Case 1, the reference group, the nozzle height was set to half of the nozzle diameter and both V_n and V_m were designed to 30 mm/s, aiming for a V_n/V_m ratio of 1. However, controlling V_m precisely was challenging, as it was influenced not only by the rotational speed of the auger screw but also by the amount of material in the hopper and the time-dependent rheological behaviours of the mortar. To mitigate this, the rotational speed of the screw was adjusted via G-code, and the mortar was added to the hopper after each layer was printed to maintain a consistent volume. The V_m was recorded accurately to ensure reliable data. The parametric study (Cases 2–5) examined the effects of these processing parameters on the layer shape and the concrete flow process.

To accurately determine the material extrusion speed V_m of each specimen, a novel three-step method was developed, which takes advantage of a movable print bed, as follows:

(a) Determine the mass M_i of each specimen: The print bed is weighed as M_{bed} before printing. After printing each specimen, the combined mass of the print bed and the printed specimens $M_{bed} + M_1 + M_2 + \ldots + M_n$ is measured. The massof each specimen M_i is then calculated by $M_i = (M_{bed} + M_1 + M_2 + \ldots + M_i) - (M_{bed} + M_1 + M_2 + \ldots + M_{i-1})$.

(b) Calculate the volume of each specimen by $V_i = M_i / \rho$, where ρ is the density of the mortar.

(c) Calculate the average material inlet speed of each specimen by $V_m = V_i/t_i$,where t_i is the printing time of each specimen.

All 3DCP experiments were conducted in a ventilated indoor laboratory with an ambient temperature of approximately 25 °C. Before starting the tests, the auger screw, hopper, and nozzle were lubricated with a thin paste of cement and water. The mortar was prepared in a single batch by mixing the solid materials for 1.5 minutes, adding water over 30 seconds, and then mixing for an additional 4 minutes. 10 minutes after mixing, the mortar was manually fed into the hopper of the auger screw assembly and printed onto the print bed. Before formal printing, a trial extrusion was performed to discharge the lubricated paste layer and to verify the printability of the mortar. The full printing process for ten specimens lasted approximately 7.5 minutes, with about 30 seconds per layer. To prevent drying, the printed segments were covered with a wet cloth. After 1.5 hours, both ends of each segment were cut to remove the effects of unstable extrusion, as shown in Fig. 4. Note that cutting the specimens too early might result in deformation since the mortar is still soft at the initial setting stage while cutting too late makes the hardened material difficult to cut manually.

To precisely capture the cross-sectional geometry of the 3D-printed specimens, their widths and heights were carefully measured using a vernier calliper. Additionally, all cross-sectional cuts were digitised and analysed using a custom image processing script that employed OpenCV and Matplotlib, as shown in Fig. 5. The process began by rotating and centring the images before clipping them. The clipped images were then converted to grayscale, smoothed using a Gaussian blur, and processed with Canny edge detection to outline

(a) The 3D PotterBot Super 10 concrete printer (b) The auger screw assembly

Fig. 2. The 3D concrete printer system.

Table 1
Settings of main process parameters in 3DCP tests.

Case	Nozzle move velocity V_n (mm/s)	Material inlet velocity V_m (mm/s)	V_n/V_m	Nozzle height H_{nozzle} (mm)
1	30	33.4	0.90	12.7
2	30	37.8	0.79	12.7
3	40	27.1	1.48	12.7
4	40	36.3	1.10	12.7
5	30	32.7	0.92	19.05
6	30	29.3	1.02	12.7
7	30	35.1	0.86	12.7
8	40	26.5	1.51	12.7
9	40	36.1	1.11	12.7
10	30	31.4	0.96	19.05

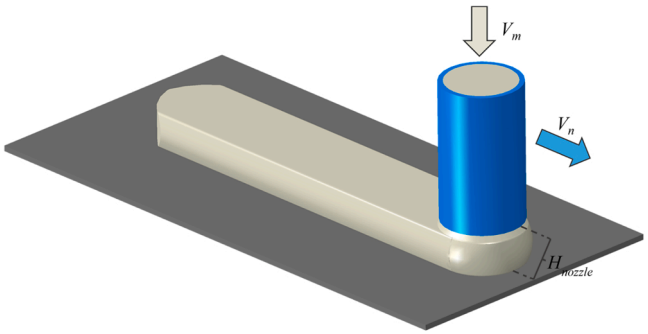

Fig. 3. Schematic of 3DCP process.

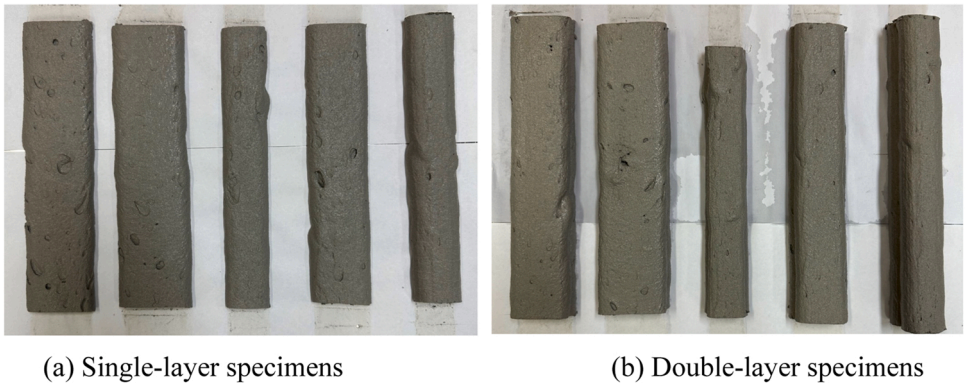

Fig. 4. The cut 3D printed mortar specimens (Cases 1–10, from left to right).

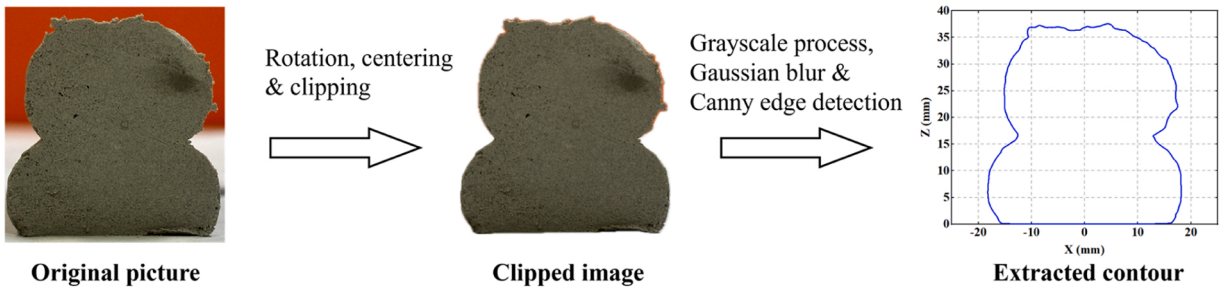

Fig. 5. Image processing script.

and draw the contours.

2.3. SPH modelling of 3DCP process

2.3.1. SPH governing equations

The main equations to be solved in SPH method are the incompressible mass and momentum conservation equations, alongside the constitutive relation of the viscous fluid. Since that the only acting body force is gravity, the Navier-Stokes equations can be expressed as [11]:

$$\nabla \cdot \boldsymbol{v} = 0 \tag{1}$$

$$\rho \frac{D\boldsymbol{v}}{Dt} = -\nabla P + \nabla \cdot \boldsymbol{\tau} + \rho g \tag{2}$$

where ∇ denotes the divergence operator, $\boldsymbol{v}$ is the velocity vector field, ρ is density, P represents the pressure in a Lagrangian frame, $\boldsymbol{\tau}$ represents deviatoric stress tensor, and g is gravity.

In the SPH method, the fluid is discretised into a collection of particles [25]. Each particle carries mass, density, and velocity. Their influence on neighbouring particles is determined by a smoothing kernel function, as illustrated in Fig. 6 [29]. This kernel function is typically chosen to be a cubic spline due to its numerical stability. It enables the transformation of the governing differential equations into integral forms, which are solved based on particle interactions within a finite support radius, known as the smoothing length.

In this study, the smoothing length of the cubic spline kernel was automatically calculated at the start of the analysis by Abaqus [32]. This ensures that each particle interacts with enough neighbours, typically between 50 and 60, within the influence range of the kernel function. To improve numerical stability, especially in high-velocity regions, artificial viscosity was applied following the method proposed in [15]. Throughout the simulation, particles were dynamically tracked to accurately capture fluid behaviours over time. This approach ensures the robustness and precision required for simulating complex 3D concrete printing processes.

2.3.2. Material models

The Bingham model was adopted to describe the rheological behaviour of fresh mortar [33]. Using the generalised Newtonian fluid model, the constitutive relationship can be expressed as:

$$\boldsymbol{\tau} = 2\eta_a \dot{e} = \eta_a \dot{\gamma} \tag{3}$$

where, $\boldsymbol{\tau}$ is the deviatoric stress, η_a is the apparent viscosity, $\dot{e}$ is the deviatoric part of the strain rate, and $\dot{\gamma} = 2\dot{e}$ is the engineering shear strain rate.

To prevent numerical singularities at low shear rates where the viscosity tends to infinity, the viscosity function is regularised using a bi-viscous model:

$$\eta_a = \begin{cases} \eta_{\max} if \ \dot{\gamma} < \dot{\gamma}_c \\ \frac{\tau_0}{\dot{\gamma}} + \eta_p if \dot{\gamma} \geq \dot{\gamma}_c \end{cases} \tag{4}$$

where, $\dot{\gamma}_c$ is the regularisation critical shear rate, τ_0 is the yield stress, η_p is the plastic viscosity, and $\eta_{\max} = \frac{\tau_0}{\dot{\gamma}_c} + \eta_p$ is the cutoff maximum value of the regularised viscosity function. In this study, to maintain a balance between computational accuracy and efficiency, $\dot{\gamma}_c = 0.01\ s^{-1}$ was used, giving a maximum cutoff viscosity of $\eta_{\max} = 29kPa \bullet s$.

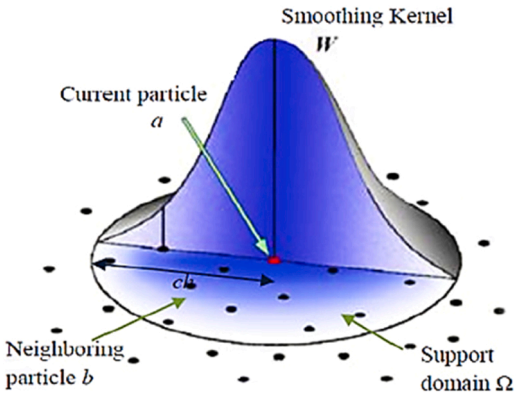

Fig. 6. Particle approximations using smoothing kernel [25].

2.3.3. Geometric models

The SPH model was devised using Abaqus/CAE to consist of a mortar particle generator, an extrusion nozzle, and a print bed as depicted in Fig. 7. The nozzle was modelled as a cylindrical tube with an inner diameter of 25.4 mm, a wall thickness of 2.0 mm, and a length of 50 mm, the same as those in the experiments. The mortar particle generator was positioned at the top surface of the nozzle, where it generates mortar particles with defined material properties, particle radius and material inlet velocity V_m. The nozzle and generator remained stationary while the print bed was assigned to move at a steady velocity V_n. In a steady extrusion, the two opposite configurations, where the nozzle moved and the printing bed was fixed, and vice versa, are equivalent [34]. The nozzle height H_{nozzle} was kept constant. After the extrusion, the material was only subjected to gravitational forces. Table 2 summarises the 3DCP process parameters used in the devised SPH models.

2.3.4. Boundary conditions

To solve the mass and momentum conservation equations, appropriate initial boundary conditions were established. A no-slip boundary condition was imposed on the print bed and nozzle walls, as the surface roughness of nozzle walls is comparable to the sand particle size [35]. A "hard contact" was employed to avoid potential penetration of fluid particles. A common issue with the SPH method is the truncated smoothing kernel at boundaries, which can reduce the integration accuracy. When the particle approaches Lagrangian boundaries, the smoothing kernel is truncated, leaving part of its supporting domain without SPH particles. To mitigate this issue, a ghost particle method [36] was implemented to create a virtual plane with ghost particles. These ghost particles, defined by properties like pressure, density, and velocity calculated from the real particles do not interact with the cement particles but provide data for kernel interpolation near the boundaries.

2.3.5. Meshing and solving

SPH mortar particles were modelled using 1-node continuum particle (PC3D) elements with a 1-mm mesh size. This size was chosen based on a mesh sensitivity analysis that compared three mesh sizes of 0.75 mm, 1 mm, and 1.5 mm. Fig. 8 illustrates the variation in strain energy over the printing time for three mesh sizes. The extracted strain energy curves clearly show that three mesh sizes provided matched results throughout the simulation process, though the curve for the mesh size of 1.5 mm was slightly lower than the others. Moreover, Fig. 9 shows the predicted layer geometries for Case 3 using the three particle sizes, while Fig. 10 compares the corresponding layer contours with experimental measurements. The mesh sizes of 0.75 mm and 1 mm both provide accurate geometric predictions, while the 1.5-mm mesh result exhibits larger deviations with a lower resolution. Consequently, the 1-mm mesh size was adopted to ensure sufficient resolution to capture the layer shape while maintaining computational efficiency.

The nozzle and print bed were treated as rigid body, with a smaller mesh size of 0.5 mm used to prevent fluid particle penetration. Despite the finer mesh, the computational cost remained low due to the rigid body treatment. The single-layer printing model consisted of approximately 10,000 SPH mortar particles and 250,000 grid cells, while the double-layer model used around 18,000 SPH particles.

Explicit dynamic analysis was used to simulate the concrete flow. The time-step size was automatically adjusted by the solver based on numerical stability and convergence criteria, mainly influenced by the effective plastic viscosity and the cubic spline kernel function.

All simulations were run in parallel on a high-performance workstation with 32 cores available at Western Sydney University. Computational CPU times for the single-layer and double-layer printing simulations were approximately one day and three days, respectively. By increasing the mortar mesh size to 1.5 mm, the computational time of the single-layer SPH model can be reduced to 9.5 hours, at the cost of a lower but acceptable resolution.

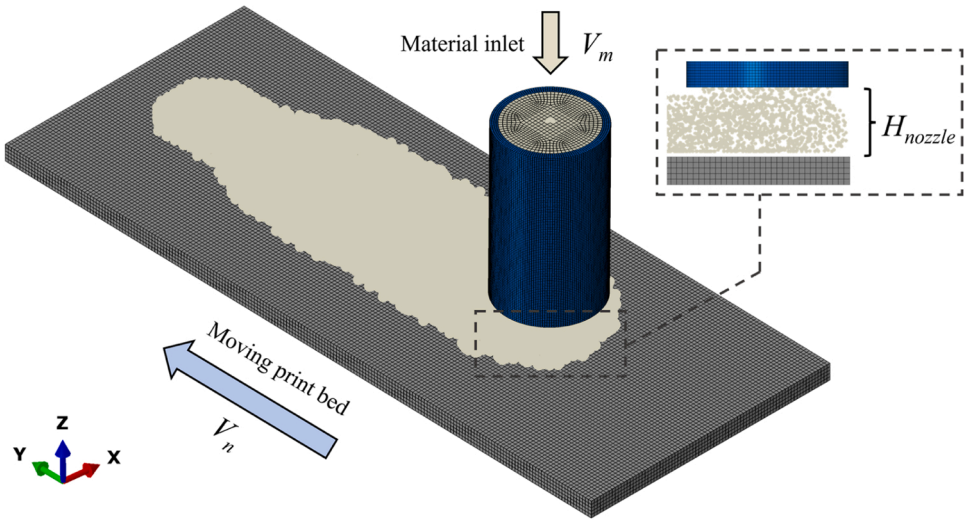

Fig. 7. The devised SPH model of 3DCP process.

Table 2
3DCP process parameters used in SPH models.

Parameters	Numerical values
Nozzle diameter D	25.4 mm
Nozzle height H_n	12.7 and 19.05 mm
Printing speed V_n	30 and 40 mm/s
Material inlet velocity V_m	See values in Table 1

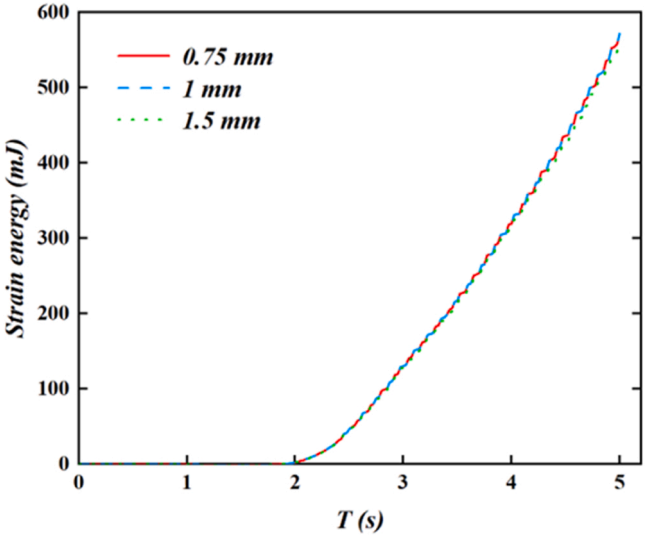

Fig. 8. The mesh sensitivity analysis.

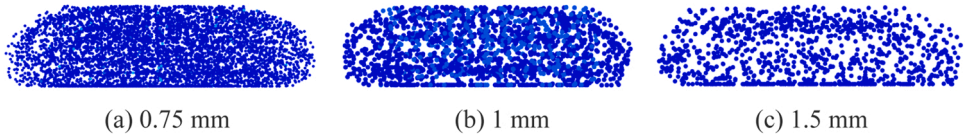

Fig. 9. The middle planes of simulated layer with various particle sizes.

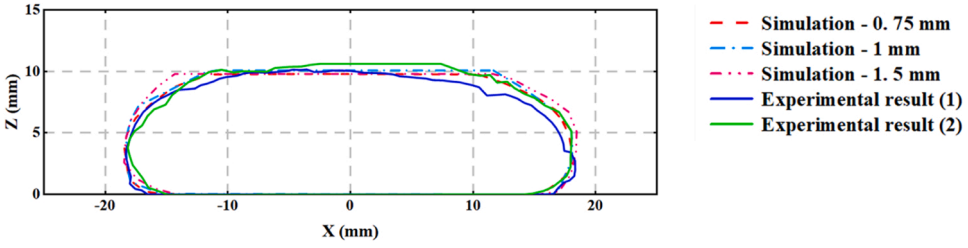

Fig. 10. The layer contours with various particle sizes and experimental measurements.

3. Results and discussion

3.1. Rheological behaviours of fresh mortar

The obtained results of the flow curve tests are shown in Fig. 11. The torque-speed data were converted into shear stress (τ) and shear rate (γ) curves using the Reiner-Riwlin equations and linear regression with least-squares minimization was applied to analyse the data [37]. According to the Bingham model [11], the vertical intercept of the flow curves represents the yield stress, while the slope of the fitted line corresponds to the plastic viscosity. For the three mortar batches tested, the average dynamic yield stress was determined to be 290.3 Pa, and the plastic viscosity was 6.5 Pa·s.

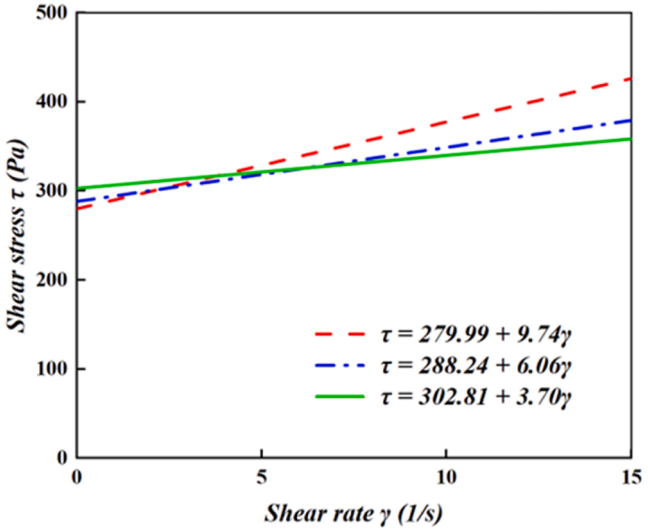

Fig. 11. The shear stress - shear rate curve of the mortar.

In the constant shear rate tests, the static yield stress was derived from the maximum torque recorded, with an average value of 894.2 Pa across three tests. The measured mortar density was 2057.8 kg/m^3 . Given the short printing duration (~7.5 minutes) and continuous shearing action of the single-screw extruder, the flocculated particle structures and early hydration products in the mortar are likely disrupted, reducing the in-process yield stress to a level comparable to that measured at 15 minutes. This supports the use of 15-minute rheological parameters in the SPH simulations.

3.2. Experimental and numerical results of 3DCP tests

Fig. 12 show the process and method to compare the experimental and 3-D SPH numerical results. The printing processes of ten 3D printed concrete specimens were simulated using the developed SPH model. Cross-sectional shapes of the numerical results were obtained by slicing the simulated layer geometries along their middle planes as shown in the right of this figure.

The geometric dimensions of 3D printed layers, including both experimental measurements and numerical predictions, are summarised in Tables 3 and 4. Fig. 13 compares the cross-sectional shapes from the experiments and numerical simulations for the ten segments. Overall, the numerical results (dashed red line) closely align with the experimental outcomes (solid blue and green lines), validating the SPH modelling approach.

In single-layer printing (Cases 1–5), the differences in layer height and width are minimal, with deviations below 1.5 mm and discrepancies generally within ±5 %, demonstrating the high accuracy of the model. In the double-layer printing (Cases 6–10), deviations range from 1.0 to 2.5 mm with most relative errors below 10 %, showing reasonable accuracy despite reduced predictive performance with more layers. Given that 3DCP operates at a metre scale [11], this variation remains within an acceptable range.

For the double-layer printing, the simulated layers appear flatter, with lower height and greater width, whereas the experimental results show a more rounded geometry. The discrepancy may be attributed to increased dynamic yield stress during printing, driven by structuration accelerated under ambient temperatures around 25 °C, especially in GGBFS-based mortars. However, as the current Abaqus SPH framework does not support defining contact between different SPH materials, it is not doable to assign distinct rheological histories to individual layers. As a result, a uniform and constant yield stress is applied to all particles. This simplification neglects time-dependent stiffening in previously deposited layers, leading to underestimated resistance and overpredicted deformation, thereby reducing the accuracy of multi-layer simulations. Another contributing factor may be minor fluctuations in the cross-sectional shape of the experimental specimens, possibly due to filament buckling or nozzle vibration, while the simulations generally produce smoother layer shape.

3.3. Effect of V_n/V_m on layer shape and inter-layer deformation

Fig. 14 (a) and (b) illustrate how the layer dimensions, width W and height H, changes with the ratio of nozzle moving velocity and material inlet velocities V_n/V_m under a nozzle height of 12.7 mm. Regarding the single-layer segments, as the V_n/V_m ratio increases from 0.79 to 1.48, the layer width decreases by 37.04 % (from 58.10 mm to 36.58 mm), while the height decreases by 16.6 % (from 12.35 mm to 10.3 mm). These reductions occur because a higher V_n/V_m ratio means less concrete is extruded per unit length of the print bed, as noted in literature [11]. Additionally, the greater reduction in width (37.04 %) compared to height (16.6 %) indicates that V_n/V_m has a more pronounced effect on width than height. Essentially, when sufficient concrete is extruded, it tends to spread sideways rather than stack vertically, a phenomenon known as the "compacting effect of the nozzle" [38].

Fig. 15 shows the numerical velocity vector fields of extruded concrete near the nozzle exit, revealing distinct flow characteristics

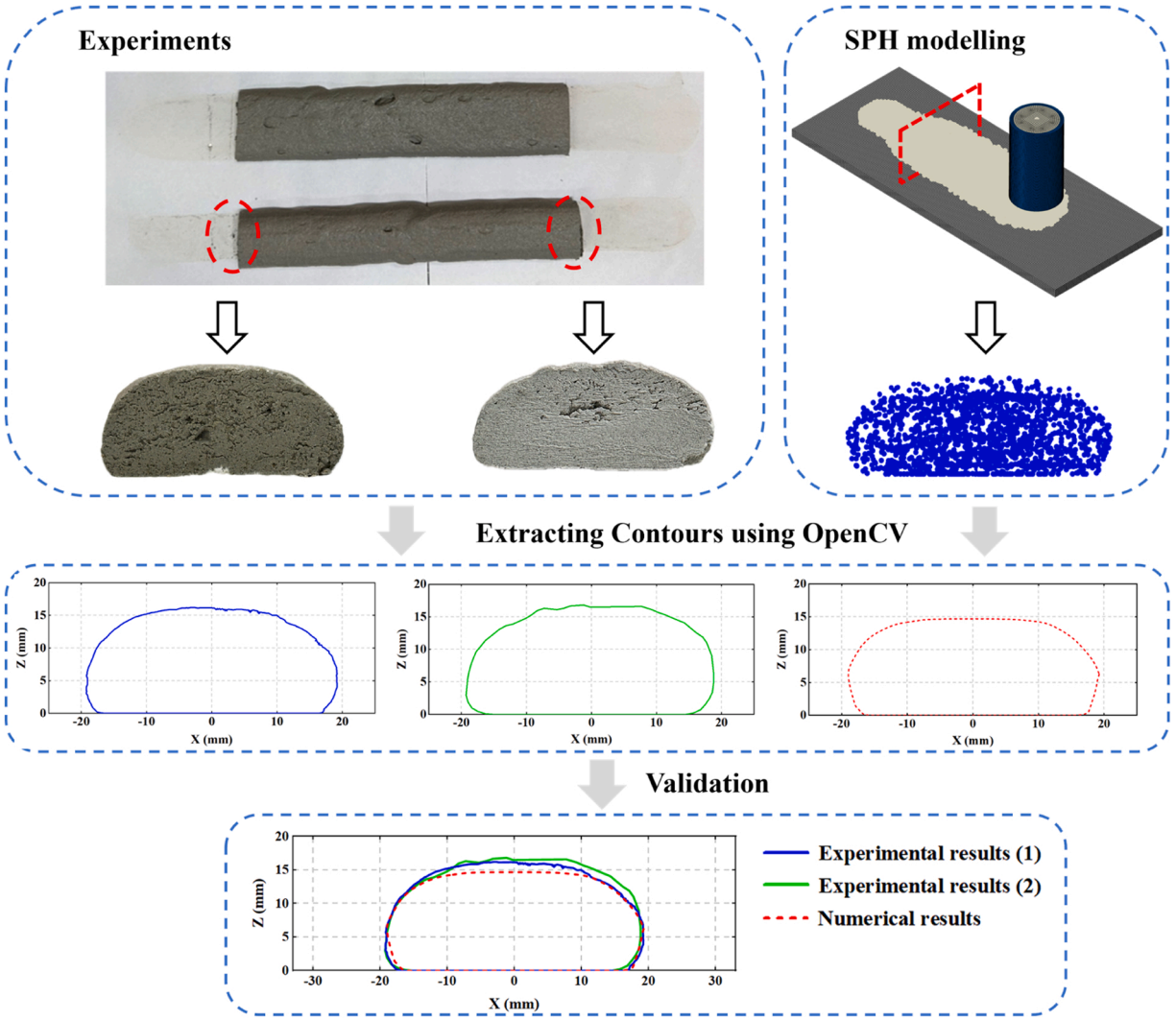

Fig. 12. The contour extraction and comparison.

Table 3
Experimental and numerical layer geometry in single-layer printing (Cases 1–5).

Case	Vn/Vm	Dimension	Section 1	Section 2	Average	Numerical Prediction	Discrepancy
1	0.90	W	56	55.8	55.9	54.85	−1.88 %
		H	11.8	12.1	11.95	11.64	−2.59 %
2	0.79	W	58.2	58	58.1	57.76	−0.59 %
		H	12.4	12.3	12.35	11.84	−4.13 %
3	1.48	W	36.65	36.5	36.575	36.35	−0.62 %
		H	10	10.6	10.3	10.07	−2.23 %
4	1.10	W	46.9	47	46.95	46.3	−1.38 %
		H	11	11.4	11.2	10.87	−2.95 %
5	0.92	W	38.35	38	38.175	38.46	+ 0.75 %
		H	16.2	16.6	16.4	14.9	−9.15 %

Note: All dimensions are reported in millimetres. The “Discrepancy” represents the relative error, calculated as the numerical prediction minus the experimental average, divided by the experimental average.

under varying V_n/V_m ratios. At low V_n/V_m, lateral expansion is evident, with velocity vectors extending outward horizontally from the nozzle base, which explains the wider layer formation associated with the compacting effect. At high V_n/V_m, the flow becomes more vertically aligned, with reduced lateral spread due to limited material supply and stronger downward momentum.

In addition to reduced material availability at high V_n/V_m, rheological effects may also influence the width reduction. Shear-

Table 4
Experimental and numerical layer geometry in double-layer printing (Cases 6–10).

Case	Vn/Vm	Dimension	Section 1		Section 2	Average	Difference	Numerical Prediction	Discrepancy
6	1.02	W_1	51.3	50.3	50.8		3.55	52.1	+ 2.56 %
		W_2	47.8		47.25			46.55	−1.48 %
				46.7					
		H_1	10.2	11.6			2	9.68	−11.19 %
					10.9				
		H_2	13.2	12.6				12.99	+ 0.70 %
					12.9				
7	0.86	W_1	56.7	54.9	55.8		2.05	58.5	+ 4.84 %
		W_2	53.9		53.75			53	−1.40 %
				53.6					
		H_1	11.2	10.6			1.8	9.68	−11.19 %
					10.9				
		H_2	12.5	12.9				13.02	+ 2.52 %
					12.7				
8	1.51	W_1	35.85	33.9	34.875		4.325	36.32	+ 4.14 %
		W_2	30.5		30.55			32.8	+ 7.36 %
				30.6					
		H_1	10.1	11			2.8	9.79	−7.20 %
					10.55				
		H_2	13.6	13.1				12.21	−8.53 %
					13.35				
9	1.18	W_1	45.1	44.3	44.7		4.2	47.73	+ 6.78 %
		W_2	40.9		40.5			40.16	−0.84 %
				40.1					
		H_1	11	11.1			2	9.99	−9.59 %
					11.05				
		H_2	13.1	13				12.52	−4.06 %
					13.05				
10	0.96	W_1	36.3	35.2	35.75		5.4	38.06	+ 6.46 %
		W_2	31		30.35			30.87	+ 1.71 %
				29.7					
		H_1	16.6	16.5			3.8	16.5	−0.30 %
					16.55				
		H_2	20.3	20.4				18.06	−11.25 %
					20.35				

Note: All dimensions are in millimetres. “Difference” refers to the variation between H_1 and H_2, and between W_1 and W_2.

induced particle migration may occur during extrusion, with particles moving from high-shear regions near the nozzle wall toward the centre, reducing particle concentration near the edges and limiting lateral spread. Moreover, localised shear thinning near the nozzle exit lowers apparent viscosity, promoting faster axial flow and restricting lateral expansion.

For double-layer specimens, as V_n/V_m increases by 43 %, from 0.85 to 1.50, the widths of the first layer W_{1st} and the second layer W_{2nd} decrease by 37.5 % and 43.2 %, from 55.8 mm and 53.75 mm to 34.875 mm and 30.55 mm, respectively. However, the height of the first layer H_{1st} fluctuates slightly between 10.55 mm and 11.05 mm, while the height of the second layer H_{2nd} increases by 4.9 %, from 12.7 mm to 13.35 mm. This suggests that V_n/V_m has a significant effect on layer width but a neglected effect on the height of double-layer specimens.

To further analyse the effect of V_n/V_m on the total height of specimens, Fig. 16 shows their relationship. The height of the single-layer specimens $H_{1\text{-}layer}$ decreases linearly as V_n/V_m increases, whereas the total height of the double-layer specimens $H_{2\text{-}layer}$ fluctuates slightly between 23.6 mm and 24.1 mm. This suggests that the volume of extruded concrete has a marginal effect on the total height of double-layer specimens compared to single-layer segments. This difference is due to the self-compensatory effect of the printed nozzle height, which becomes more pronounced when there is insufficient material at high V_n/V_m ratios. Specifically, Fig. 17 illustrates the inter-layer deformation of double-layer specimens and the self-compensatory effect of the printed nozzle height. In the designed scheme, the extruded concrete should fill in the gap between the nozzle and print bed, creating layers with uniform layer shape. However, in practice, the height of the first layer is usually slightly lower than the designed nozzle height H_{nozzle}, due to the vertical deformation of fresh concrete under gravity and the extrusion force [14]. Consequently, the practical printed nozzle height H'_{nozzle} for the second layer is higher than the designed H_{nozzle}. At higher V_n/V_m, the insufficient material beneath the printhead exaggerates this effect, resulting in a higher second layer, and therefore compensates for the height difference with specimens under lower V_n/V_m ratios.

The self-compensatory effect on upper-layer height occurs at the cost of reduced layer width due to the fixed extruded material volume. In large-scale 3DCP, this phenomenon is common in the final printed layers, where cumulative deformations raise the practical printed nozzle height H'_{nozzle} above the designed height H_{nozzle}, resulting in a rounder layer shape with an increased height but a reduced width. To mitigate this geometric discrepancy, slightly increasing the material inlet velocity V_m can compensate for the width reduction. Additionally, slicing strategies should incorporate layer width compensation to maintain printing precision and ensure structural consistency.

From Fig. 13 and Table 4, it is also evident that the difference in layer width and height between the first and second layers

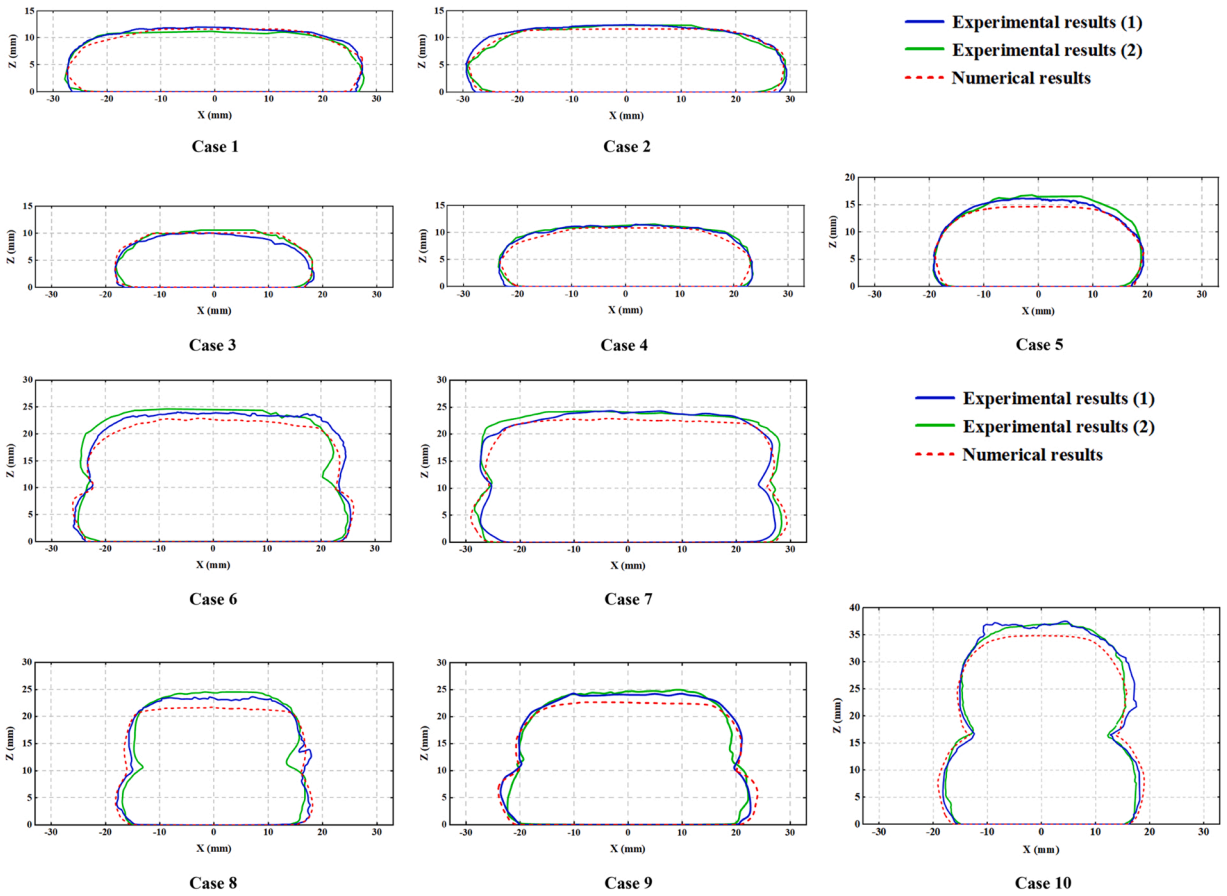

Fig. 13. Comparisons of the cross-sectional shapes of numerical and experimental results: the SPH model's high accuracy in predicting layer height and width, and the increasing discrepancies in double-layer printing due to cumulative deformations.

increases as the V_n/V_m ratio rises. This trend is highlighted in Fig. 18, which compares the cross-sectional shapes of Case 7 (V_n/V_m = 1.51) and Case 8 (V_n/V_m = 0.86). In Case 7 the difference between W_{1st} and W_{2nd} is 4.325 mm, or 12.4 %. Whereas in case 8, where the extruded material is sufficient, the difference between W_{1st} and W_{2nd} is only 2.05 mm, or 3.7 %, indicating that the two layers have nearly the same width.

The geometry difference between the first and second layers arises from the variation in their practical nozzle heights during printing. When the extruded material is insufficient, as in the case of a high V_n/V_m ratio, the practical nozzle height for the second layer is higher than the designed nozzle height. This leads to a more rounded second layer, consistent with findings in literature [8], and a larger difference from the flatter first layer. In contrast, when the material is sufficient, as with a low V_n/V_m ratio, the compacting effect of the nozzle is more pronounced, and the first layer height closely matches the nozzle height (e.g., in case 2, where V_n/V_m = 0.79, $H_{1\text{-}layer}$ = 12.35 mm, and H_{nozzle} = 12.7 mm). This ensures that the practical nozzle height for the second layer remains close to the designed height, resulting in more uniform layer shape. Thus, to achieve more consistent layer shape and improved mechanical performance in 3D printed specimens, it is recommended to use sufficient concrete (lower V_n/V_m) during printing.

3.4. Effect of nozzle height on inter-layer deformation

Fig. 13 illustrates that increasing the nozzle height results in printed layers with a more rounded cross-sectional shape, characterised by greater layer height and reduced width, consistent with the findings in literature [11,13]. To further investigate the effect of nozzle height on inter-layer deformation, single- and double-layer 3D printing processes were simulated using the proposed SPH model, with various nozzle heights (H_{nozzle} = 12.7, 15.875, 19.05, 22.225, and 25.4 mm) under a V_n/V_m ratio of 1.

Fig. 19 presents the relationship between the predicted total specimen height and nozzle height. The green and blue solid lines represent the ideal cases where the specimen height H equals the designed nozzle height ($H = H_{nozzle}$) and twice the nozzle height ($H = 2H_{nozzle}$), respectively. The gap between these solid lines and dashed lines (denoting actual total specimen height $H_{1\text{-}layer}$ and $H_{2\text{-}layer}$) reflects the extent of layer deformation. The results indicate that deformation increases with nozzle height for both single- and double-layer specimens. This is because higher nozzle heights create more rounded layers, which leads to greater layer height and increased gravitational pressure, resulting in more vertical deformation. Another factor is that at higher nozzle heights, the material is

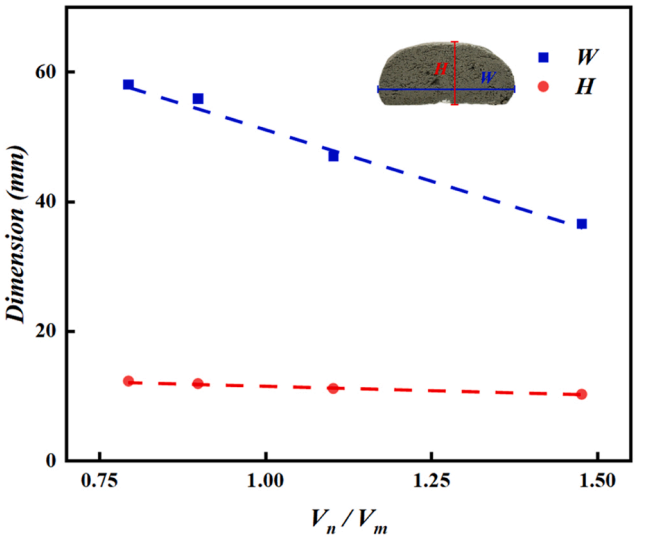

(a) Single-layer printing (Cases 1 - 4)

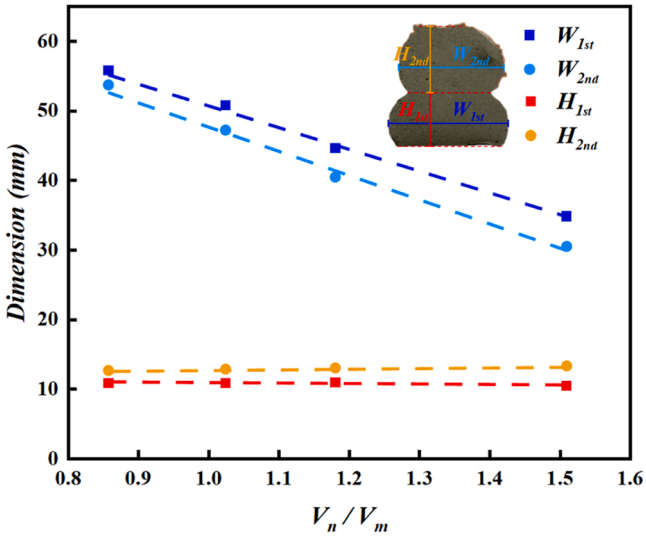

Fig. 14. The relationship between layer dimensions and V_n/V_m.

insufficient to fully fill the gap between the nozzle and the print bed since the volume of extruded concrete remains constant.

When the nozzle height exceeds 19.05 mm, double-layer specimens exhibit significantly greater deformation than single-layer ones. This is mainly because the yield stress of mortar is insufficient to resist the increased gravitational load at larger gaps. As a result, the upper layer undergoes excessive vertical deformation, while the first layer is subjected to secondary loading from the overlying material and extrusion pressure during placement of the second layer. Unlike the upper layer, which flows immediately after extrusion, the bottom layer has already entered a resting state, and it is subsequently reloaded, resulting in additional compression. This non-uniform deformation reflects dynamic stress redistribution, wherein stress from the newly extruded layer is progressively transmitted to the underlying one, leading to localised deformation differences.

In summary, increasing the nozzle height initially causes a gradual rise in the specimen height; however, once the yield stress threshold is exceeded, deformations become significantly more pronounced, leading to vertical compression of the upper layer and flattening of the lower layer. In large-scale 3DCP, where cumulative deformations tend to accumulate, monitoring practical nozzle height and implementing adaptive control are essential for maintaining consistent layer geometry.

These observed effects of V_n/V_m and nozzle height H_{nozzle} are summarised in Table 5, which highlights their respective impacts on layer width, height, and inter-layer deformation. This overview serves as a practical reference for optimising process parameters and improving print quality in 3DCP.

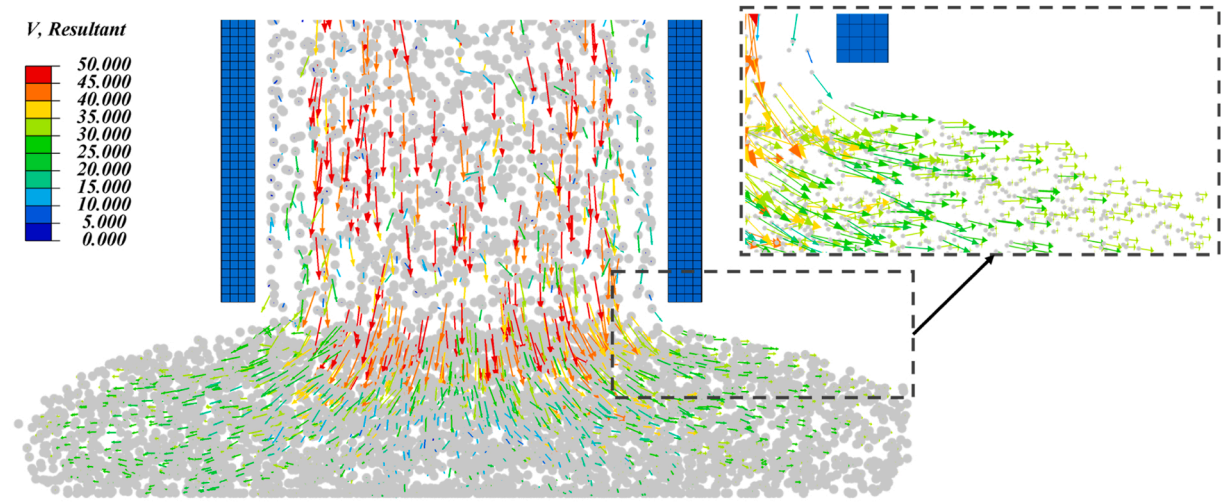

(a) Low $V_n/V_m = 0.79$, Case 2

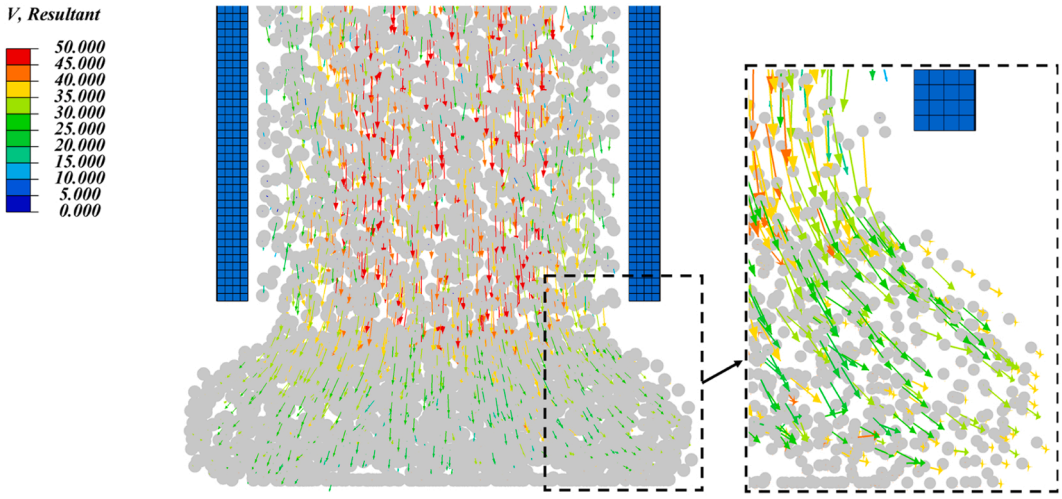

(b) High $V_n/V_m = 1.48$, Case 3

Fig. 15. Comparison of velocity vector fields under low and high V_n/V_m (Insets highlight the flow direction and lateral spread of the extrude material near the nozzle exit).

3.5. Effect of nozzle length on layer shape

The primary goal of this section is to identify a numerical solution for reducing computational time. To reduce the computational cost of developed models and investigate the effect of nozzle length on the layer shape, a series of simulations were performed using single layers with varying nozzle lengths (25, 35, 40, 45, and 50 mm). The processing parameters were set to a V_n/V_m ratio of 1 and a nozzle height of 12.7 mm. Table 6 summarises the layer dimensions and the corresponding computation time for different nozzle lengths.

The results indicate that nozzle length has a limited effect on the layer shape, with shorter nozzle lengths producing flatter cross-sectional shapes. When the nozzle length reaches 45 mm, the geometry both in shape and dimensions becomes identical to that of the 50 mm nozzle. This suggests that the nozzle length of 45 mm can be considered as a critical value for simulation purposes, allowing for a 10.4 % reduction in computational time, from 2.5 hours.

The flatter cross-sections observed with shorter nozzles are due to the reduced vertical velocity of the mortar. In the SPH model, the vertical velocity is initially set to V_n and increases within the nozzle under gravitational force. During this process, the fluid pressure of concrete flow is generated and applied to the nozzle. The fluid pressure is released once the concrete is extruded, and a horizontal velocity vector forms, causing the concrete to spread laterally.

It is important to note that determining the critical nozzle length analytically is a complex issue involving pipe rheology and the

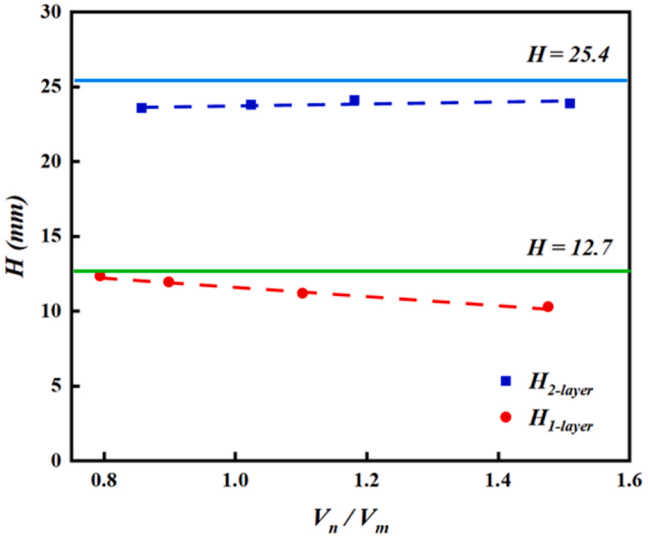

Fig. 16. The relationship between specimen height and V_n/V_m.

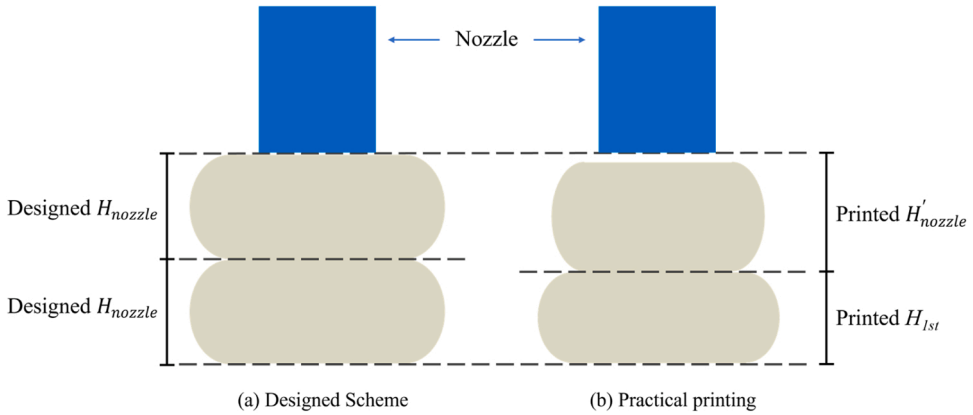

Fig. 17. The typical inter-layer deformation in 3DCP.

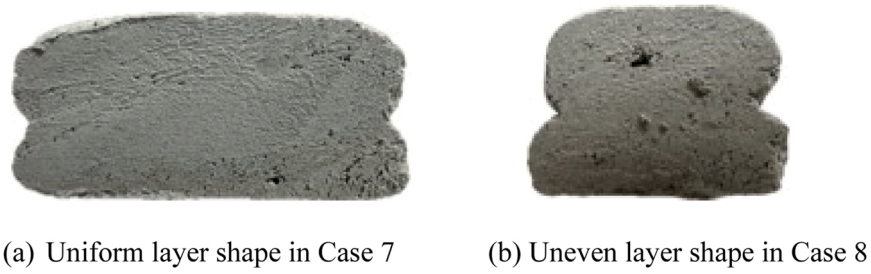

Fig. 18. The layer geometrical difference caused by various V_n/V_m.

reaction force of the print bed, which lies beyond the scope of this study.

4. Conclusion

The integrated framework of the experimental and 3-D SPH modelling analysis of 3DCP has been developed in this research. The experimental program was conducted to characterise the rheological properties of fresh concrete for the numerical modelling of 3D concrete printing. Ten single- and double-layer concrete samples were 3D printed using various processing parameters. Subsequently,

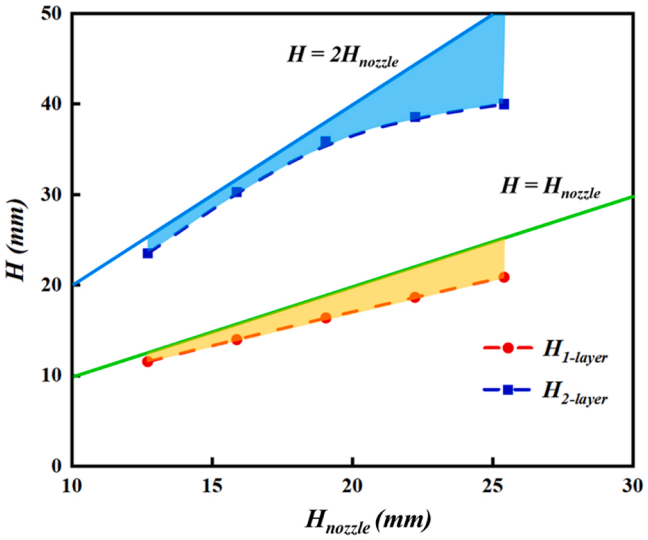

Fig. 19. The relationship between the specimen height and nozzle height.

the novel 3-D SPH method was developed to simulate the 3D printing process of both single and double-layer concrete samples. Moreover, the effects of two key processing parameters including the ratio of nozzle velocity to material inlet velocity and nozzle height on layer shape and inter-layer deformations were examined both experimentally and numerically.

Based on the obtained results, the following conclusions can be drawn.

- Based on both experimental and numerical results, the ratio of nozzle moving velocity to material inlet velocity V_n/V_m significantly affects layer shape, particularly the width and evenness of double-layer specimens. However, its impact on total height is mitigated by the self-compensatory effect of nozzle height. A lower ratio (0.85–1) is recommended for achieving uniform layer shape and improved mechanical performance.
- Based on both experimental and numerical results, higher nozzle height results in a rounder layer shape – larger height and smaller width. The specimen total height increases with the nozzle height within the limitation of material yield stress. Excessive nozzle height, however, can lead to material yielding and excessive deformation.
- In large-scale 3DCP, cumulative deformations in the final printed layer may elevate the practical nozzle height, leading to a rounder shape with an increased height and a reduced width. To mitigate this, optimising slicing strategies, such as slightly increasing material inlet velocity, applying width compensation in slicing software, and implementing adaptive height control, helps maintain print accuracy and geometric consistency.
- The developed 3-D SPH model can accurately predict the layer shapes of both single- and double-layer 3D printed concrete specimens. It captures the inter-layer deformation behaviours of the samples and reveals a self-compensatory effect of nozzle height on layer height, thereby reducing the discrepancy between the overall height of the printed structure and the intended design.
- Through the parametric studies using the devised SPH model, a nozzle length of 45 mm can be considered a critical value in numerical simulations, reducing computational time by 10.4 %.

Overall, the developed SPH models effectively simulate single- and double-layer 3D printing processes, providing accurate predictions of cross-sectional shapes. However, challenges remain in simulating large-scale 3DCP due to high computational demands and the limitations of current models in capturing time-dependent rheological and mechanical behaviours. In particular, the time-dependent increase in yield stress due to material structuration was not considered in this study, as the current Abaqus SPH framework does not support contact between different SPH materials. This limitation necessitates the use of a uniform and constant yield stress across all layers, which may reduce the accuracy of multi-layer SPH simulations. Currently, no existing model fully accounts for both the rheological and mechanical behaviours in large-scale concrete 3D printing, highlighting the complexity of this task. The next step in advancing this research is to integrate SPH with the Finite Element Method (FEM), incorporating a time-dependent elastic-viscoplastic constitutive model to simulate large concrete structures and optimally set the 3DCP at large scale, driving the broader application of 3DCP-based technologies in modern building engineering construction.

CRediT authorship contribution statement

Yang Richard (Chunhui): Writing – review & editing, Supervision, Resources, Methodology, Conceptualization. **Rahman Mahfuzur:** Validation, Investigation. **An Dong:** Writing – original draft, Investigation, Formal analysis, Data curation. **Zhang Y.X.:** Writing – review & editing, Supervision, Methodology.

Table 5
The effects of V_n/V_m and H_{nozzle} on layer geometry and inter-layer deformation.

	Layer shape	Inter-layer deformation
V_n/V_m	A higher V_n/V_m reduces the layer width and height both. Width reduction is more significant due to compacting effect of the nozzle.	A higher V_n/V_m leads to specimen height fluctuation due to the self-compensatory effect of nozzle height. It also results in worse layer geometric consistency.
H_{nozzle}	A higher H_{nozzle} increases the layer height but reduces the width.	A higher H_{nozzle} increases specimen vertical deformation. Excessive H_{nozzle} may cause material yielding and severe deformation.

Table 6
Layer dimensions and computing time using different nozzle lengths.

Nozzle length (mm)	25	35	40	45	50
W (mm)	50.9	50.5	50.1	49.8	49.8
H (mm)	11.1	11.3	11.5	11.6	11.6
Computing time (hour)	15.5	18.5	19.75	21.5	24

Declaration of Competing Interest

The authors declare that they have no known competing financial interests or personal relationships that could have appeared to influence the work reported in this paper.

Acknowledgements

The first author acknowledges the PhD scholarship funded by the China Scholarship Council (CSC) and Graduate Research School (GRS), Western Sydney University. Technical supports from the Teaching & Research Technical Services (TRTS) at Western Sydney University are appreciated.

Data availability

Data will be made available on request.

References

[1] V. Mechtcherine, V.N. Nerella, F. Will, M. Näther, J. Otto, M. Krause, Large-scale digital concrete construction–CONPrint3D concept for on-site, monolithic 3D-printing, Autom. Constr. 107 (2019) 102933.
[2] G. Murali, L.S. Wong, Waste-driven construction: a state-of-the-art review on the integration of waste in 3D printed concrete in recent researches for sustainable development, J. Build. Eng. (2024) 111268.
[3] J. Cao, E. Shengzhao, Y. Yang, Y. Shi, J. Chai, Z. Xu, A strategy for the improvement of the bonding performance of 3D-printed concrete interlayer interfaces, J. Build. Eng. 97 (2024) 110675.
[4] M. Rahman, S. Rawat, R. Yang, A. Mahil, Y. Zhang, A comprehensive review on fresh and rheological properties of 3D printable cementitious composites, J. Build. Eng. (2024) 109719.
[5] D. An, Y. Zhang, R. Yang, Incorporating coarse aggregates into 3D concrete printing from mixture design and process control to structural behaviours and practical applications: a review, Virtual Phys. Prototyp. 19 (1) (2024) e2351154.
[6] D. An, Y. Zhang, R.C. Yang, Numerical modelling of 3D concrete printing: material models, boundary conditions and failure identification, Eng. Struct. 299 (2024) 117104.
[7] G. Duarte, J.P. Duarte, N. Brown, A. Memari, J.P. Gevaudan, Design for early-age structural performance of 3D printed concrete structures: a parametric numerical modeling approach, J. Build. Eng. 94 (2024) 109986.
[8] R.J. Wolfs, T.A. Salet, N. Roussel, Filament geometry control in extrusion-based additive manufacturing of concrete: the good, the bad and the ugly, Cem. Concr. Res. 150 (2021) 106615.
[9] R. Comminal, M.P. Serdeczny, N. Ranjbar, M. Mehrali, D.B. Pedersen, H. Stang, J. Spangenberg, Modelling of material deposition in big area additive manufacturing and 3D concrete printing. Joint Special Interest Group Meeting between Euspen and ASPE Advancing Precision in Additive Manufacturing, The European Society for Precision Engineering and Nanotechnology, 2019, pp. 151–154.
[10] Z. Liu, M. Li, Y. Weng, Y. Qian, T.N. Wong, M.J. Tan, Modelling and parameter optimization for filament deformation in 3D cementitious material printing using support vector machine, Compos. Part B: Eng. 193 (2020) 108018.
[11] R. Comminal, W.R.L. da Silva, T.J. Andersen, H. Stang, J. Spangenberg, Modelling of 3D concrete printing based on computational fluid dynamics, Cem. Concr. Res. 138 (2020) 106256.
[12] J. Reinold, V.N. Nerella, V. Mechtcherine, G. Meschke, Extrusion process simulation and layer shape prediction during 3D-concrete-printing using the Particle Finite Element Method, Autom. Constr. 136 (2022) 104173.
[13] Y. Wei, S. Han, Z. Chen, J. Lu, Z. Li, S. Yu, W. Cheng, M. An, P. Yan, Numerical simulation of 3D concrete printing derived from printer head and printing process, J. Build. Eng. 88 (2024) 109241.
[14] Y. Wei, S. Han, S. Yu, Z. Chen, Z. Li, H. Wang, W. Cheng, M. An, Parameter impact on 3D concrete printing from single to multi-layer stacking, Autom. Constr. 164 (2024) 105449.
[15] V. Nguyen-Van, S. Li, J. Liu, K. Nguyen, P. Tran, Modelling of 3D concrete printing process: A perspective on material and structural simulations, Addit. Manuf. 61 (2023) 103333.
[16] S.A. Khan, M. Koç, Numerical modelling and simulation for extrusion-based 3D concrete printing: The underlying physics, potential, and challenges, Results Mater. 16 (2022) 100337.
[17] K. El Abbaoui, I. Al Korachi, M. El Jai, B. Šeta, M.T. Mollah, 3D concrete printing using computational fluid dynamics: modeling of material extrusion with slip boundaries, J. Manuf. Process. 118 (2024) 448–459.
[18] H. Cheng, A. Radlińska, M. Hillman, F. Liu, J. Wang, Modeling concrete deposition via 3D printing using reproducing kernel particle method, Cem. Concr. Res. 181 (2024) 107526.
[19] J. Reinold, K. Daadouch, G. Meschke, Numerical simulation of three dimensional concrete printing based on a unified fluid and solid mechanics formulation, Front. Struct. Civ. Eng. (2024) 1–25.
[20] G. Rizzieri, L. Ferrara, M. Cremonesi, Numerical simulation of the extrusion and layer deposition processes in 3D concrete printing with the Particle Finite Element Method, Comput. Mech. 73 (2) (2024) 277–295.
[21] G. Rizzieri, M. Cremonesi, L. Ferrara, A 2D numerical model of 3D concrete printing including thixotropy, Mater. Today.: Proc. (2023).
[22] R. Jayathilakage, P. Rajeev, J. Sanjayan, Extrusion rheometer for 3D concrete printing, Cem. Concr. Compos. 121 (2021) 104075.
[23] H. Yu, W. Zhang, B. Yin, W. Sun, A. Akbar, Y. Zhang, K. Liew, Modeling extrusion process and layer deformation in 3D concrete printing via smoothed particle hydrodynamics, Comput. Methods Appl. Mech. Eng. 420 (2024) 116761.
[24] J. Spangenberg, W.R.L. da Silva, R. Comminal, M.T. Mollah, T.J. Andersen, H. Stang, Numerical simulation of multi-layer 3D concrete printing, RILEM Tech. Lett. 6 (2021) 119–123.

[25] G.-R. Liu, M.B. Liu, Smoothed Particle Hydrodynamics: A Meshfree Particle Method, World Scientific, 2003.
[26] H.T. Thanh, J. Li, Y. Zhang, Numerical simulation of self-consolidating engineered cementitious composite flow with the V-funnel and U-box, Constr. Build. Mater. 236 (2020) 117467.
[27] H.T. Thanh, J. Li, Y. Zhang, Numerical modelling of the flow of self-consolidating engineered cementitious composites using smoothed particle hydrodynamics, Constr. Build. Mater. 211 (2019) 109–119.
[28] W. Alyhya, S. Kulasegaram, B. Karihaloo, Simulation of the flow of self-compacting concrete in the V-funnel by SPH, Cem. Concr. Res. 100 (2017) 47–59.
[29] D. Yang, K. Wu, L. Wan, Y. Sheng, A particle element approach for modelling the 3D printing process of fibre reinforced polymer composites, J. Manuf. Mater. Process. 1 (1) (2017) 10.
[30] E. Bertevas, J. Férec, B.C. Khoo, G. Ausias, N. Phan-Thien, Smoothed particle hydrodynamics (SPH) modeling of fiber orientation in a 3D printing process, Phys. Fluids 30 (10) (2018).
[31] E.P. Koehler, D.W. Fowler, Development of a portable rheometer for fresh portland cement concrete, 2004..
[32] G. Abaqus, Abaqus 6.11, Dassault Systemes Simulia Corporation, Providence, RI, USA, 2011, p. 3.
[33] N. Roussel, Rheological requirements for printable concretes, Cem. Concr. Res. 112 (2018) 76–85.
[34] M.P. Serdeczny, R. Comminal, D.B. Pedersen, J. Spangenberg, Experimental validation of a numerical model for the strand shape in material extrusion additive manufacturing, Addit. Manuf. 24 (2018) 145–153.
[35] N. Roussel, A. Gram, Simulation of fresh concrete flow. RILEM State-of-the-Art Reports, Springer, Dordrecht, The Netherlands, 2014.
[36] R.A. Gingold, J.J. Monaghan, Smoothed particle hydrodynamics: theory and application to non-spherical stars, Mon. Not. R. Astron. Soc. 181 (3) (1977) 375–389.
[37] H. Gao, L. Jin, Y. Chen, Q. Chen, X. Liu, Q. Yu, Rheological behavior of 3D printed concrete: influential factors and printability prediction scheme, J. Build. Eng. 91 (2024) 109626.
[38] G. Ji, J. Xiao, P. Zhi, Y.-C. Wu, N. Han, Effects of extrusion parameters on properties of 3D printing concrete with coarse aggregates, Constr. Build. Mater. 325 (2022) 126740.